

Model-Based THz Imaging for 2D Reflection-Mode Geometry

Malakeh A. Musheiness¹, Charles J. Divin¹, Jeffrey A. Fessler¹, and Theodore B. Norris¹

¹FOCUS Center and Center for Ultrafast Optical Science, University of Michigan,

2200 Bonisteel Boulevard, Ann Arbor, Michigan 48109-2099

Author e-mail address: mmushein@umich.edu

Abstract: We demonstrate 2D reflection-mode THz imaging with model-based reconstruction. A substantial improvement in the reconstruction of objects is obtained via the model-based algorithm compared to the time-reversal algorithm.

©2010 Optical Society of America

OCIS codes: (110.6795) Terahertz imaging; (100.3010) Image reconstruction techniques

1. Introduction

THz image reconstruction techniques such as tomography and time-reversal are alternative methods to direct scanning of objects used by most THz imaging systems [1-2]. Recently, we have shown that model-based imaging yields a substantial improvement over the time-reversal technique in the reconstruction of time-reversed scattered fields for one-dimensional transmission geometries [3]. Here, we demonstrate the applicability of model-based imaging to 2D reflection-mode geometries. By using the actual impulse response of the THz system in the model-based algorithm, we can significantly improve the quality of the reconstructed images compared to the time-reversal method; in particular, reconstruction artifacts due to the non-ideal impulse response are greatly suppressed.

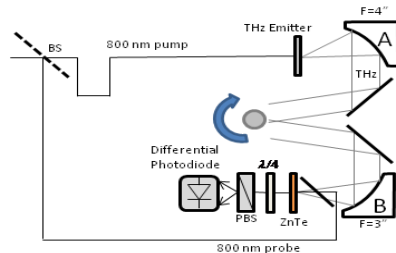


Fig.1. Experimental setup for reflection mode geometry

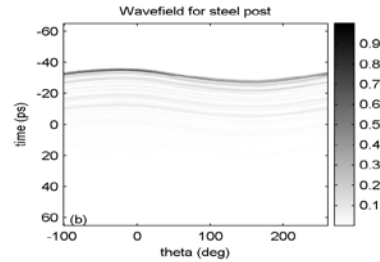


Fig. 2. Wavefield plot for steel post

2. Experiment

The experimental setup, as illustrated in Fig.1, is a typical electro-optic THz imaging system operating in reflection mode [4]. Femtosecond pulses are split into pump and probe; the pump illuminates a large-area photoconductive emitter (TeraSED, GigaOptics GmbH) to generate a nearly single cycle THz pulse. The THz beam is collimated by a parabolic mirror, A, with a focal length of 102 mm. The first of the two metal coated mirrors in between the parabolic mirrors directs the collimated THz beam onto the object while the second mirror directs a portion of the scattered THz onto a second parabolic mirror, B, of focal length 76 mm for electro-optic detection in the ZnTe crystal by the probe [4]. The object imaged is a 12.66 mm steel post which was mounted onto a rotation stage and rotated in increments of 2 degrees for a full revolution. We chose the steel post as our object for its simplicity, anticipating that if the center of the post rotated about the pivot point, we should expect a flat wavefield plot as a function of angle. However, the wavefield plot in Fig. 2 shows that the post was slightly off center.

3. Analysis

To model our system, we began by first discretizing our object plane into a rotating grid of possible point scatters. Each point can reflect a portion of the incident THz beam. We model the detected signal as a superposition of those reflections convolved with the impulse response of our THz system. Hence we can express the observed signal at the angular position θ as

$$S_{\theta}(t) = \sum_{i=1}^N \sum_{j=1}^N R(x_i, z_j) h(t - \tau_{x_i, z_j, \theta}), \quad \text{where} \quad \tau_{x_i, z_j, \theta} = \frac{x_i \sin(\theta + \alpha) + z_j \cos(\theta + \alpha) + x_i \sin(\theta - \alpha) + z_j \cos(\theta - \alpha)}{c} \quad (1)$$

Here $R(x_i, z_j)$ denotes the unknown value of the object's reflectivity at the grid point (x_i, z_j) , α is the angle of the incident THz beam with respect to the normal, c is the speed of light, and $h(t)$ is the impulse response of the THz system that is delayed by a known parameter $\tau_{x_i, z_j, \theta}$ with respect to the pivot point. The rotating geometry and the

plane wave detection of our THz setup are captured by the delay parameter $\tau_{x_i, z_i, \theta}$. By ordering our grid points and concatenating our observed signals (i.e. Fig. 2), we can cast the equation (1) into matrix form as $\mathbf{Y}=\mathbf{A}\mathbf{R}$ where \mathbf{Y} is a vector consisting of observed signals, \mathbf{A} is a known system matrix, and \mathbf{R} is a vector of unknown parameters. We obtain an estimate for \mathbf{R} by minimizing the following regularized least squares (RLS) cost function

$$\hat{R} = \underset{R}{\operatorname{argmin}} \|Y - AR\|^2 + \beta \sum_{m=2}^{N^2} (R(x_m, z_m) - R(x_{m-1}, z_{m-1}))^2 \quad (2)$$

The first term in the above equation encourages a best fit of the measured data while the second term discourages disparities in the neighboring pixel values. The parameter β controls the tradeoff between the two and controls the balance between spatial resolution and noise in the final estimate [5].

We implemented a 2D reconstruction algorithm based on the RLS criterion given in Eq. (2) and compared its performance to that of the time-reversal algorithm, using the data of Fig. 2. After four iterations, the model-based algorithm achieved a better reconstruction of the steel post than did the time reversal. As evidenced by the reconstructed images shown in Fig. 3a and 3b, normalized to their respective peaks, we see that both algorithms reconstructed the cross section of the steel post with the right dimensions of 12.7 mm. However, the model-based image clearly shows that the grid points corresponding to points inside the steel post are very close to zero. However, the time reversal algorithm clearly has artifact signals inside the perimeter of the post. Thus the image produced by the model-based algorithm is qualitatively more consistent with the object than the time-reversal. We can quantify the improvement of the model-based algorithm versus the time-reversal algorithm by integrating the reconstructed images azimuthally and plotting the resulting signals as a function of radius as shown in Fig. 3c and 3d. From the plots we calculated a peak SNR (in amplitude) for the model-based algorithm of 80.0 and a peak SNR of 16.9 for the time-reversal algorithm. Hence, the model-based algorithm has resulted in a factor of approximately 5 (14 dB) improvement in SNR over the time-reversal algorithm.

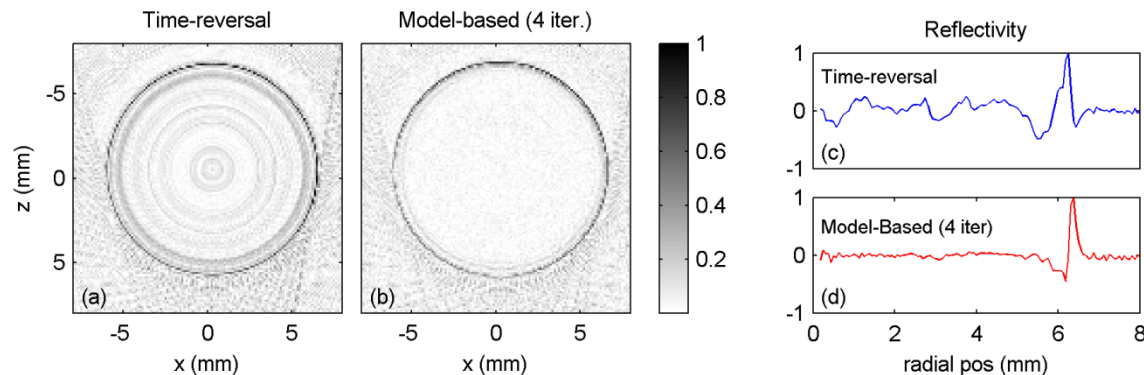


Fig.3. Image reconstruction of steel post via a) time-reversal b) model-based. Azimuthally integrated images as a function of radius via time-reversal c) and via model-based d).

4. Conclusion

In summary, we have shown the feasibility of model-based THz image reconstruction for 2D reflection-mode geometries. Furthermore, we have shown that the model-based algorithm achieves a better and more consistent reconstruction of objects than the time reversal algorithm with very few iterations, and with an improvement in the peak SNR of approximately 5 (14 dB). We expect further improvements via more iterations, a better choice for β , and a more accurate measurement of α .

5. References

- [1] D. M. Mittleman, M. Gupta, R. Neelamani, R.G. Baranuik, J.V. Rudd, and M. Koch, "Recent advances in terahertz imaging," *Appl. Phys. B* **68**, 1085-1094 (1999).
- [2] A. B. Ruffin, J. V. Rudd, J. Decker, L. Sanchez-Palencia, L. Le Hors, J. F. Whitaker, and T. B. Norris, "Time Reversal Terahertz Imaging," *IEEE J. Quantum Electron.* **38**, 1110-1119 (2002).
- [3] M. A. Musheesh, C. J. Divin, J. A. Fessler, and T. B. Norris, "Time-reversal and model-based imaging in a THz waveguide," *Opt. Express* **17**, 13663-13670 (2009).
- [4] T. Buma and T.B. Norris, "Coded excitation of broadband terahertz using optical rectification in poled lithium niobate," *Appl. Phys. Lett.* **87**, 251105-251105-3 (2005).
- [5] J. A. Fessler, "Penalized Weighted Least-Squares Image Reconstruction for Positron Emission Tomography," *IEEE Trans. Med. Imag.*, **13**, 290-300 (1994).